Discoveries

Forum Review Article

Pulsed Electron Paramagnetic Resonance Imaging: Applications in the Studies of Tumor Physiology

Shun Kishimoto,[1] Ken-Ichiro Matsumoto,[2] Keita Saito,[1] Ayano Enomoto,[1] Shingo Matsumoto,[3] James B. Mitchell,[1] Nallathamby Devasahayam,[1] and Murali C. Krishna[1]

Abstract

Significance: Electron paramagnetic resonance imaging (EPRI) is capable of generating images of tissue oxygenation using exogenous paramagnetic probes such as trityl radicals or nitroxyl radicals. The spatial distribution of the paramagnetic probe can be generated using magnetic field gradients as in magnetic resonance imaging and, from its spectral features, spatial maps of oxygen can be obtained from live objects. In this review, two methods of signal acquisition and image formation/reconstruction are described. The probes used and its application to study tumor physiology and monitor treatment response with chemotherapy drugs in mouse models of human cancer are summarized.

Recent Advances: By implementing phase encoding/Fourier reconstruction in EPRI in time domain mode, the frequency contribution to the spatial resolution was avoided and images with improved spatial resolution were obtained. The EPRI-generated pO_2 maps in tumor were useful to detect and evaluate the effects of various antitumor therapies on tumor physiology. Coregistration with other imaging modalities provided a better understanding of hypoxia-related alteration in physiology.

Critical Issues: The high radiofrequency (RF) power of EPR irradiation and toxicity profile of radical probes are the main obstacles for clinical application. The improvement of RF low power pulse sequences may allow for clinical translation.

Future Directions: Pulsed EPR oximetry can be a powerful tool to research various diseases involving hypoxia such as cancer, ischemic heart diseases, stroke, and diabetes. With appropriate paramagnetic probes, it can also be applied for various other purposes such as detecting local acid–base balance or oxidative stress. *Antioxid. Redox Signal.* 28, 1378–1393.

Keywords: EPR, hypoxia, cancer, imaging, oxygen

Introduction

THE PARTIAL PRESSURE OF OXYGEN (pO_2) in tissues is strictly controlled in healthy organs. Hemoglobin bound to oxygen (oxyhemoglobin) perfuses and delivers oxygen to tissues (13). The hemoglobin affinity for oxygen changes depending on several factors such as low pH or high carbon dioxide (CO_2) and releases oxygen in favor of hypoxic tissues. The vasodilation in such tissues also compensates for the shortage of oxygen delivery (7). However, in pathophysiological states of many diseases, the homeostasis of oxygen supply/consumption balance is not maintained, resulting in low pO_2. Cancers, inflammation, and ischemic diseases are associated with low pO_2. Especially in cancer, oxygen deficiency is reported to not only promote processes driving malignant progression and metastasis but also increases the resistance toward treatment, including radiation and chemotherapy (11, 23–25, 52, 57, 63). Thus, quantitative assessment of pO_2 in the tissues can characterize such tissues and help making decision in the choice of optimal treatment strategies.

Electron paramagnetic resonance (EPR) oximetry is currently being investigated by several groups for small animal imaging applications. Because most spin probes used in EPR have relatively large line widths (LWs), continuous wave

[1]Radiation Biology Branch, Center for Cancer Research, National Cancer Institute, National Institutes of Health, Bethesda, Maryland.
[2]Quantitative RedOx Sensing Team, Department of Basic Medical Sciences for Radiation Damages, Chiba, Japan.
[3]Division of Bioengineering and Bioinformatics, Hokkaido University, Sapporo, Japan.

(CW) methods using phase-sensitive detection were preferred for signal detection. Such spectroscopic studies have been shown to be useful to obtain information on the pO_2 levels in tumors. CW L-band electron paramagnetic resonance imaging (EPRI) and spectroscopic studies have also provided information on cardiac ischemia and tumor hypoxia (2, 19, 20, 31, 33, 36, 62). The recent availability of single line paramagnetic spin probes based on the trityl radical (3) that are nontoxic, biocompatible, and water soluble made pulsed EPRI as a useful technique in preclinical research with potential for clinical translation. The information obtained from *in vivo* EPR studies such as tissue redox status or oxygen level provides a better understanding in physiological status. Radiofrequency EPRI systems operating in time domain (TD) employ narrow excitation pulses (50–100 ns), and the free induction decay (FID) signals that last typically for 1–3 μs are captured. The advantages of pulsed EPR system includes the minimal motion artifacts and short imaging times. Unlike MRl, EPRI depicts images of accumulated spin probes just as in positron emission tomography (PET). Extremely low background noise level in EPRI describes organ images clear with sufficient delineation. Our previous studies (37, 38, 40, 58, 59) have shown that *in vivo* oximetry information can be obtained with adequate image resolution and sensitivity by pulsed EPR (also known as TD EPR or Fourier transform [FT] EPR) imaging modality. In this review, the fundamentals of EPR signal acquisition and imaging and examples of applications in the studies of tumor physiology are presented.

EPR Spectroscopy and Imaging

EPR signal acquisition can be performed in the CW mode in the frequency domain or in the TD. CW EPR is suitable for species such as nitroxyls that have LWs >0.5 Gauss, whereas the TD EPR method is optimal for narrow line paramagnetic species such as the solid LiPc or the trityl radicals. EPRI both in the CW and pulsed methods can be done by frequency encoding, wherein the projections are collected and transformed to the frequency domain and image reconstructed by filtered back projection (Fig. 1A). This was used effectively in various EPRI experiments for spatial imaging and spectroscopic imaging. To map spectral information with EPRI, spectral–spatial EPRI methods are used (34, 35), wherein incrementation of unidirectional field gradient is performed to obtain a set of projections, and reconstruct image onto a 2D–4D spectral–spatial pseudo matrix using filtered back projection and/or iterative reconstruction techniques (Fig. 1B). Although FT EPRI was implemented using frequency encoding and projection reconstruction initially (Fig. 1A), significant dead times and the relatively large LWs compromised the image quality. With concepts from solid state nuclear magnetic resonance microscopy of phase encoding by collecting a single point in the TD and monitoring its phase modulation by the imposed gradients, the frequency contribution to the spatial resolution was avoided and significantly improved images in terms of spatial resolution were obtained (Fig. 1C) (58).

Principle of TD Single Point Imaging EPR Oximetry

Magnetic resonance imaging (MRI) uses the T_1 and T_2 of contrast agents to distinguish different types of tissue based on proton relaxation time differences. In blood oxygen level dependent (BOLD) MRI (6, 49–51), the differential oxygenation of hemoglobin during functional activation of the brain and the consequent magnetic susceptibility difference that depends on the ratio of hemoglobin to deoxyhemoglobin change the local relaxation time to produce the contrast. Molecular oxygen itself is a paramagnetic species with two unpaired electrons, and can also shorten proton T_1. T_1-weighted signal enhancement induced by tissue oxygen is known as tissue oxygen level dependent (TOLD) MRI signal (37). However, BOLD and/or TOLD MRI can sense qualitative changes in oxygen concentration, that is, oxygenation or deoxygenation, but do not directly measure oxygen concentration quantitatively.

The most important physiological function that is unique to EPRI is the possibility of performing oximetry based on the line broadening of spin probe LW by O_2 (15, 16, 60, 67). In EPR, dissolved oxygen acts as a natural T_2-contrast agent. EPR oximetry is based on EPR line broadening caused by shortening in spin–spin relaxation time (T_2) due to spin–spin interaction between the paramagnetic spin probe and molecular oxygen. The LW is inversely related to transverse relaxation time, T_2, or the decay time of the FID, that is, T_2^*. Since the images are processed from projections obtained by the FT of the FIDs by progressively deleting the early part of the FID, one can impart a spatially resolved T_2^*-dependent intensity attenuation in the images, thus performing a TD equivalent of spectral–spatial imaging. In other words, intensity from voxels that have maximum pO_2 will decay the fastest, whereas least oxygenated voxels will show a longer persistence due to longer T_2^*. Oxygen concentration in the sample can be quantitatively estimated by measuring the EPR LW of the probe (38). A linear relation exists between the EPR LW and oxygen concentration.

Electron paramagnetic resonance imaging

The principle of spectroscopic imaging with TD EPR using the single point imaging (SPI) modality is outlined in earlier reports (38, 58, 59). The FID following the excitation pulse is sampled using a fast analog–digital converter (500 mega samples/s; Fig. 2A). FIDs are acquired under static magnetic field gradients and the phase at a single time point is monitored as the orthogonal gradients are looped in a Cartesian space by gradual incrementation from a negative to positive value (Fig. 2B). The phase changes acquired at a given time point (τ_p) in the set of FIDs collected resemble a gradient-echo response in the transverse magnetization (Fig. 2C) from a typical MRI scan and complete spatial information can be recovered by Fourier transformation (Fig. 2D). A spectral–spatial image or T_2^* map can be reconstructed using a set of 1D spatial profiles obtained from several different τ_p. Two-dimensional or three-dimensional imaging can be achieved by using a combination of two or three orthogonal field gradients. To improve the accuracy of data, SPI can be carried out at multiple different gradient steps. Figure 3 shows the scheme of generating three sets of images with three different gradient steps: one with large gradient steps for early time points after the pulse, intermediate steps for mid range of the FID, and small steps for larger delays from the pulse. The image data are gathered in an interleaved manner to average out any spin concentration fluctuations due to pharmacokinetic clearance.
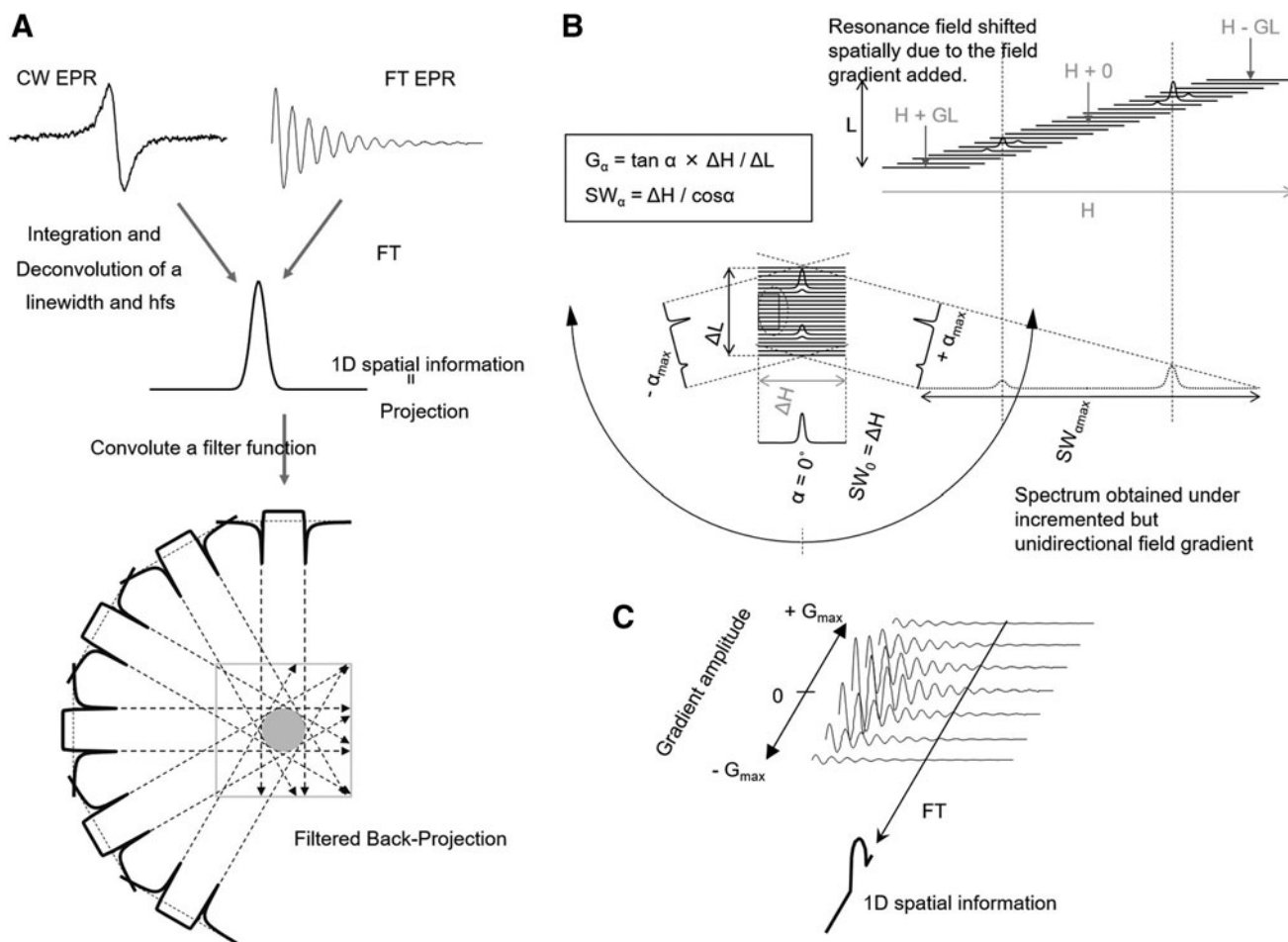
A

CW EPR   FT EPR

Integration and
Deconvolution of a   FT
linewidth and hfs

1D spatial information
=
Projection

Convolute a filter function

Filtered Back-Projection

B

$G_\alpha = \tan\alpha \times \Delta H / \Delta L$

$SW_\alpha = \Delta H / \cos\alpha$

Resonance field shifted
spatially due to the field
gradient added.

H - GL

H + 0

H + GL

L

H

$-\alpha_{max}$

ΔL

ΔH

$\alpha = 0°$

$SW_0 = \Delta H$

$+\alpha_{max}$

$SW_{\alpha max}$

Spectrum obtained under
incremented but
unidirectional field gradient

C

Gradient amplitude

$+ G_{max}$

0

$- G_{max}$

FT

1D spatial information

FIG. 1. **Schematic drawing of theory of several EPRI modalities.** (**A**) Spatial imaging using a back projection image reconstruction. The projection data are collected using rotating but a constant magnitude of field gradient. (**B**) Spectral–spatial 2D imaging in frequency domain. The projection data are collected using unidirection but incrementing magnitude of field gradient. G, magnitude of field gradient (Gauss/cm); ΔH and ΔL, spectral and spatial window width of the pseudo spectral–spatial matrix; SW, sweep width; α, viewing angle on the pseudo spectral–spatial matrix; H, magnetic field; L, spatial length. SW is varied depending on the α. Rotating field gradient direction achieves 3D or 4D imaging. (**C**) Spectral–spatial imaging in time domain. Data are collected using incrementing field gradient strengths and a constant time window (sweep width in frequency domain). Fourier transformation along G axis gives a spatial profile. With combinations of two or three orthogonal field gradient set, 3D or 4D imaging is available. EPRI, electron paramagnetic resonance imaging.

By using Oxo63 solution phantoms equilibrated with known oxygen concentration for calibration, one can generate oximetric images of the tumor-bearing organs from the *in vivo* image data. It can be seen in Figure 4 that the LW derived from SPI from the phantoms is linear with pO$_2$, and reproducible when the resonator size, filling factor, and the gradient magnitudes are kept constant.

The observed total LW (LWt) can be described by the following equation:

$$LWt = LWi + LWuh + LWg + LWc + LWo, \quad [1]$$

in which LWi is the intrinsic spin packet line width, LWuh is the contribution of unresolved hyperfine interactions of the unpaired electron with neighboring magnetic nuclei, LWg is the gradient-induced line broadening, LWc is the spin probe concentrations-dependent line width, and LWo is the oxygen-dependent line width. LWi and LWuh can be

assumed constant and LWc can be ignored at low spin probe concentration (<3 mM). Figure 4A shows the intensity change as a function of the concentration of the spin probe, wherein a linear response is noticed (38) and Figure 4B shows the relationship between LW and probe concentration. As can be seen from the inset, minimal broadening at concentrations <3 mM was noticed. Above this concentration, a concentration-dependent increase was observed. No importance was given to LWc in the pO$_2$ calculation in the following studies on the assumption of the intratumor Oxo63 concentration of not exceeding 3 mM (38). Figure 4C shows the results of the pulsed EPRI using SPI for LW mapping of a four-tube phantom containing 3 mM Oxo63 with different levels of pO$_2$. A linear correlation between LW broadening and oxygen concentration, which determines the relationship of LWo with pO$_2$, is shown in Figure 4D with minimal fluctuations over the cross section.

The feasibility of *in vivo* EPR oximetry was also tested using tumor-bearing mouse (40). Figure 5A and B shows the
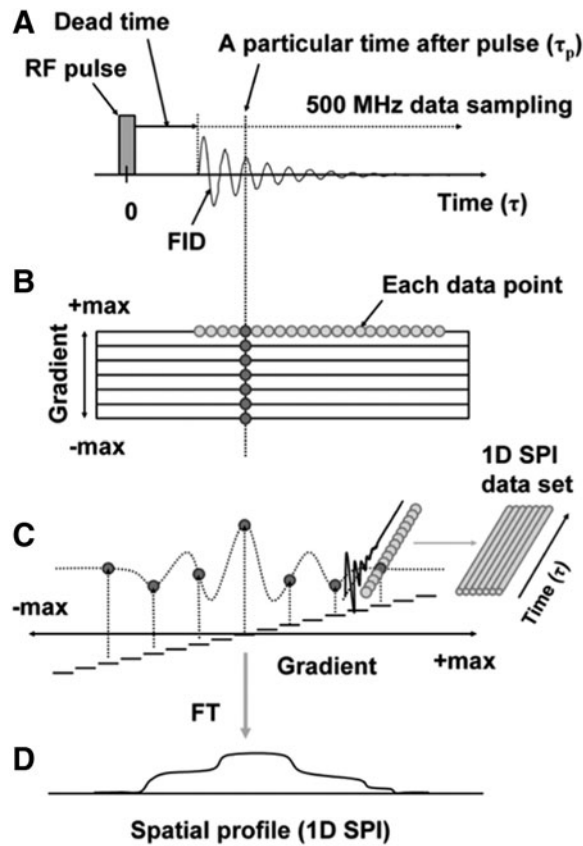
FIG. 2. Schematics of SPI. (A) The FID after the excitation pulse is digitized using a fast ADC (500 mega samples/s). (B) The gradients are systematically incremented from a negative maximum to a positive maximum. (C) The phase imparted on any particular time point (τ_p) of the set of FID simulates a gradient–echo response in the transverse magnetization. A set of FID data was saved for FT image reconstruction. Each time point of the FID set contains the full image information. (D) A 1D spatial profile, that is, 1D SPI, was obtained by FT. ADC, analog–digital converter; FID, free induction decay; FT, Fourier transform; SPI, single point imaging. Adapted from Ref. (38) with permission.

FIG. 3. Estimation of pixelwise pO_2 from SPI data sets. An SPI data set was reassembled from several SPI data sets obtained by using multiple Gmax settings. Pixels of reconstructed FID are replotted semilogarithmically. The slope of the semilogarithmical plot of the FID gives T_2^*. The EPR LW can be calculated from T_2^*. The pO_2 value can be obtained from the EPR LW using a calibration curve. Finally, pO_2 values are rearranged onto a matrix. EPR, electron paramagnetic resonance; pO_2, partial pressure of oxygen; LW, line width. Adapted from Ref. (38) with permission.

anatomic images (T_2-weighted MRI images) and corresponding pO_2 maps taken from healthy mouse (top row) and squamous cell carcinoma SCCVII tumor-bearing mouse (bottom row). The results showed that the normal muscle tissue is homogeneously well oxygenated (20.8 ± 3.3 mmHg; $n = 6$) while significant lower pO_2 level was observed (10.5 ± 3.6 mmHg; $n = 6$; $p < 0.01$) in tumor region (Fig. 5C). The results are consistent with previous reports showing that the SCC tumor at a size of 1 cm^3 exhibits significant hypoxia in a large fraction (30, 38). Figure 5D and E shows images from the same tumor-bearing mouse when the breathing gas was switched from air to carbogen (95% O_2 + 5% CO_2). The pO_2 maps from EPRI show that a significantly large part of the tumor exhibited pO_2 increase after the changing gas described in Figure 5F. The results support the capability of EPRI to distinguish a 3- to 4-mmHg pO_2 difference and is useful to study live animals and provide useful physiological information on tumor hypoxia (44, 66).
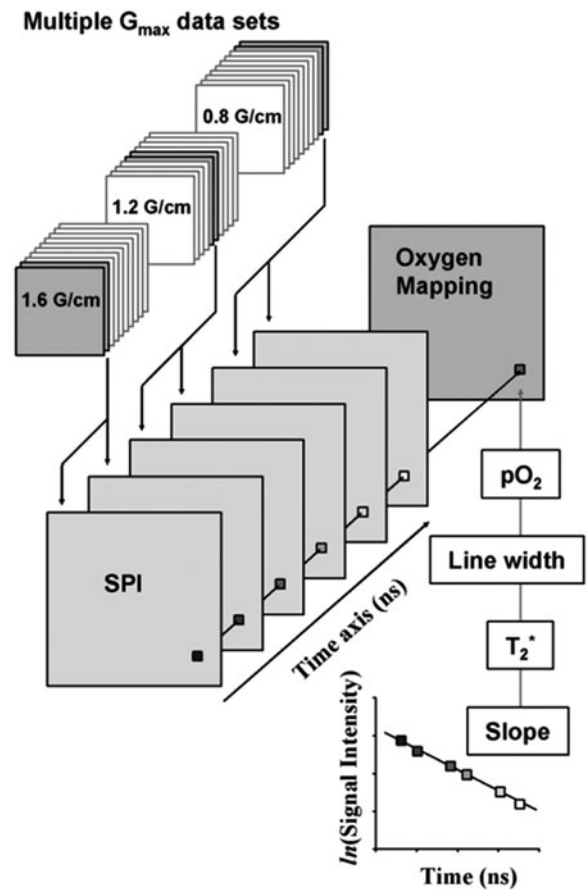
In Vivo Application of EPR Oximetry

EPRI has several intrinsic advantages when compared with other clinically available methods of assessing tumor pO_2. Polarographic measurements need an oxygen electrode insertion in the target tissue. This provides quantitative pO_2 assessments from only the needle-accessible sampling volume. In contrast, EPRI provides quantitative pO_2 values in three-dimensional maps noninvasively (66). PET, another oxygen-related imaging technique, uses a tracer that is internalized and metabolized and trapped in hypoxic regions but is not capable of providing a quantitative pO_2 information (4). In addition, EPRI can be employed to monitor temporal pO_2 fluctuations in every few minutes, whereas PET-based oxygenation assessment can only be used once for a certain time period.

Monitoring oxygen concentration in the tumor gives insights into metabolic and hemodynamic changes because these factors are closely related to oxygen delivery and consumption. Quantitative pO_2 assessment enables the comparison between different tumors with differing phenotypes at
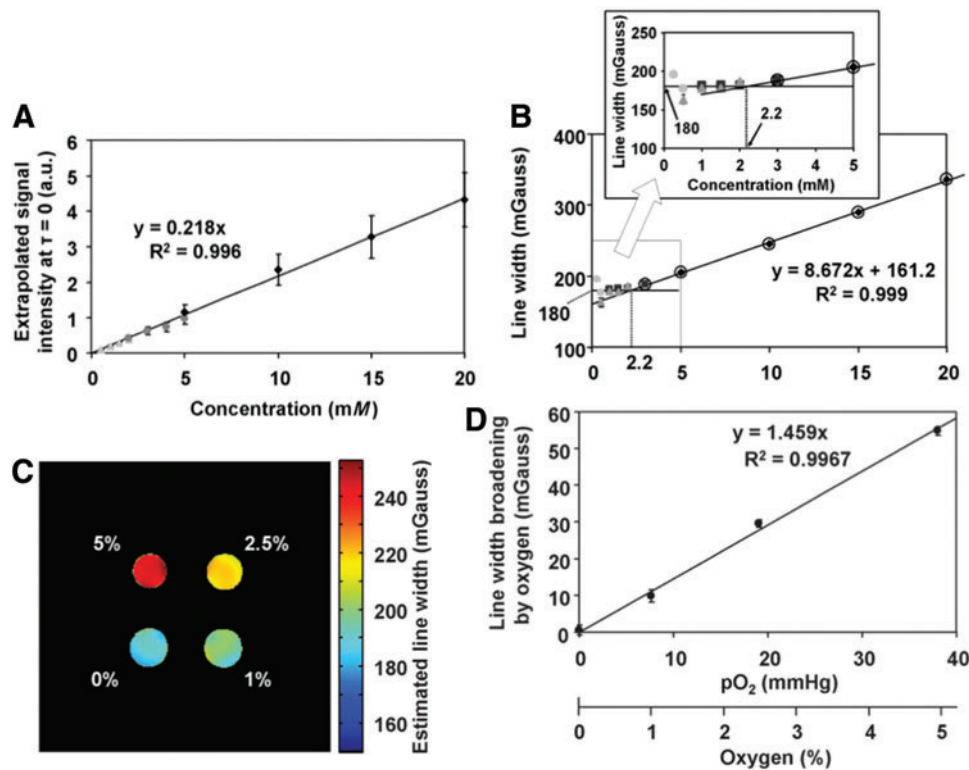
FIG. 4. Calibration curves for concentration-dependent LW broadening. **(A)** Relationship between the concentration (spin density) of Oxo63 and the extrapolated signal intensity at $\tau = 0$ ns. **(B)** Relationship between the concentration of Oxo63 and LW at 0 mmHg. Each *symbol* indicates an independent measurement. *Circles* indicate 0.25, 0.5, 1.0, and 1.5 m*M* Oxo63 solutions. *Triangles* indicate 0.5, 1.0, 1.5, and 2.0 m*M* solutions. *Squares* indicate 1.0, 1.5, 2.0, and 3.0 m*M* solutions. *Diamonds* indicate 5, 10, 15, and 20 m*M* solutions. Data points >3 m*M* (marked with *open circles*) in **(B)** were used to observe a linear equation. *Inset* shows the relationship in an expanded scale of 0–5 m*M*. Relationship between pO$_2$ and the oxygen-dependent LW broadenings. **(C)** LW mapping of a phantom containing 3 m*M* Oxo63 solutions with different oxygen levels. **(D)** Oxygen-dependent LW broadening was obtained after the correction of concentration broadening. Values are plotted as average ± SD of 374 pixels. Image acquisition time for a matrix of 31×31 size in three gradient ranges was 264 s. Adapted from Ref. (38) with permission. To see this illustration in color, the reader is referred to the web version of this article at www.liebertpub.com/ars

different time points. Noninvasive monitoring also allows us to keep track of pO$_2$ throughout studies without affecting the animal by the measurement itself. Here, we demonstrate the four main uses of EPR oximetry: (i) monitoring oxygenation kinetics in tumors, (ii) validating hypoxic cancer models, (iii) coregistration with other imaging modalities, and (iv) treatment response to anticancer therapy.

Monitoring oxygenation kinetics in tumor

Improvements of pulsed EPRI allowed high temporal and spectral resolution, which enables to monitor kinetics of oxygenation in tumor. The short scan time allows monitoring temporal changes in pO$_2$ and the sub mm^3 resolution in the image allows comparison of pO$_2$ between various regions inside of the tumor. Many solid tumors have regions with chronic and intermittent hypoxia (9, 40, 66). The phenomenon of intermittent hypoxia in tumors was reported >30 years ago and named ''cycling hypoxia'' (5, 8, 10, 12). EPRI studies were conducted to distinguish chronic and cycling hypoxic regions in a tumor. Figure 6 shows the temporal change of pO$_2$ inside murine SCCVII tumor and human colon cancer cell line HT29 tumor model (66). EPR images were

taken using the oxygen-sensitive probe Oxo63. SCCVII tumor is more hypoxic than HT29 tumor. Distinct differences were also observed in oxygenation kinetics between SCCVII tumor and HT29 tumor. Both series of oxygen maps clearly indicate fluctuating oxygen concentrations while the probe level was stable in both tumors. The magnitude of fluctuations was also different between two tumors. By examining small areas from both tumors and plotting the temporal change, it was determined that there are (i) chronic hypoxic region, (ii) acute hypoxic region, and (iii) nonhypoxic region. SCCVII tumor has more acute hypoxic regions, whereas HT29 tumor has more chronic hypoxic regions. Such studies along with the information available from earlier studies can provide improved understanding of the relationship between cycling hypoxia in treatment resistance and metastatic properties (10, 44).

Validation of hypoxia model

EPR oximetry is also utilized to study the hypoxic models of tumors in preclinical studies (29, 53, 65). EPRI allows profiling pO$_2$ across the different groups of tumors as it is quantitative. By obtaining the characteristics of tumor
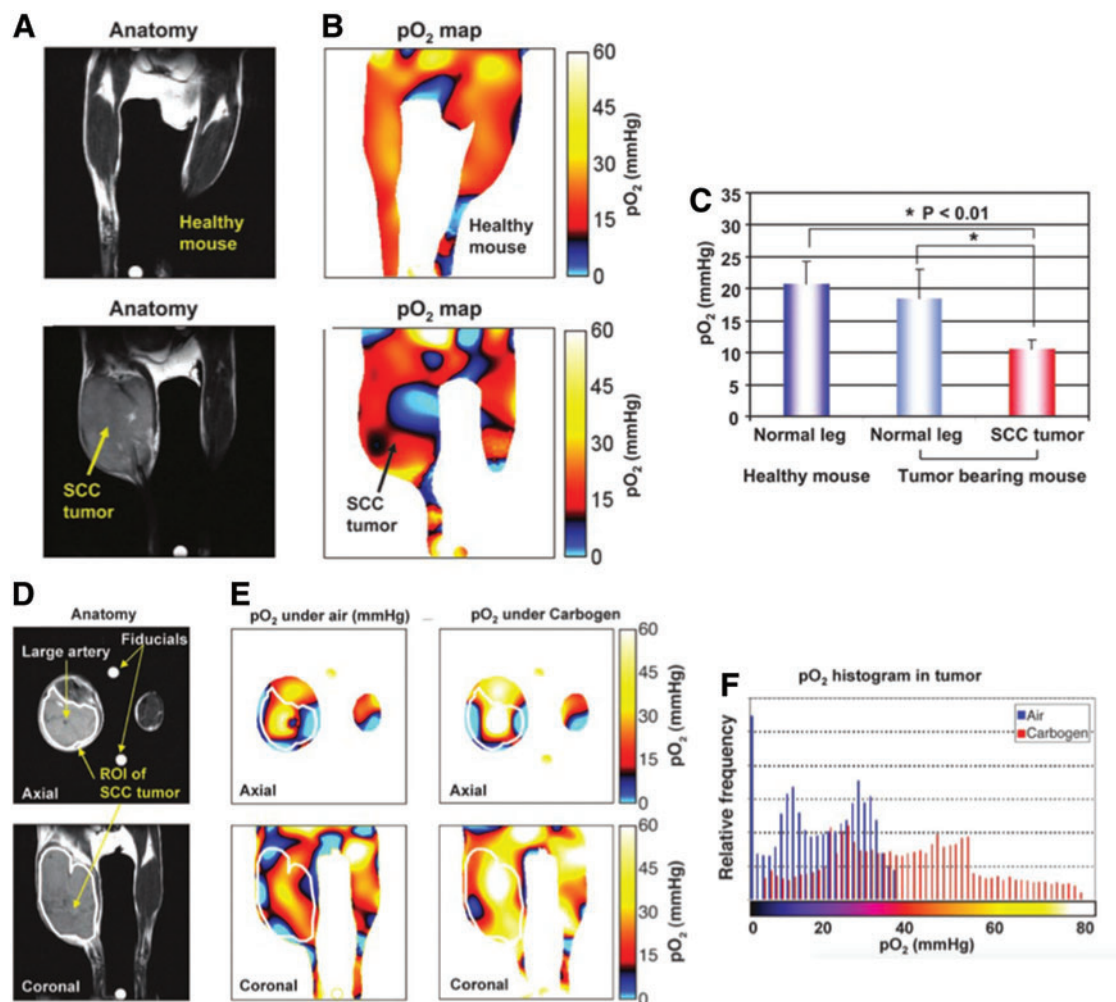
FIG. 5. Noninvasive imaging of pO_2 in healthy leg (*top*) and SCCVII tumor-implanted leg (*bottom*) using EPRI. **(A)** T_2-weighted anatomical images of a representative healthy mouse and SCCVII tumor-bearing mouse. *Yellow arrow* indicates tumor. **(B)** Corresponding pO_2 map obtained from EPRI. *Black arrow* indicates tumor. **(C)** There was no significant difference in pO_2 between normal muscle tissues with or without tumor bearing as opposed to the significant, lower pO_2 in tumor region of the SCC mouse. **(D)** T_2-weighted anatomical images of a representative SCCVII tumor-bearing mouse. *White line* indicates tumor region. **(E)** pO_2 images (axial and coronal) when breathing medical air and 30 min after carbogen breathing. **(F)** Histograms of pO_2 in the tumor region of the same mouse breathing medical air (*blue*) and carbogen (*red*). A net increase in the median pO_2 was noted upon carbogen breathing. Adapted from Ref. (40) with permission. To see this illustration in color, the reader is referred to the web version of this article at www.liebertpub.com/ars

models, the treatment responses to oxygen-dependent therapies or hypoxia targeting therapies can be predicted. Here, we describe three examples of validation studies wherein treatment outcomes were associated with the magnitudes of hypoxia in the tumors.

Radiotherapy. Figure 7 shows the comparison in therapeutic effects of radiotherapy between two tumor models in mice (53). Radiotherapy is known to be oxygen dependent because the DNA damage induced by radiotherapy is largely dependent on intracellular oxygen to fix the radiation-induced damage on the target. As shown in a previous study (Fig. 6), these tumors differ with each other in their microenvironmental oxygenation profile. Figure 7A shows representative pO_2 maps in SCCVII and HT29 tumors implanted in mouse legs. From the pO_2 maps obtained from these tumors, HF10 (fractional tumor volume with $pO_2 < 10$ mmHg)

was computed and the results are shown in Figure 7B. The results showed that the SCCVII tumor was relatively more hypoxic than the HT29 tumor. As is also shown in Figure 6, the SCCVII tumor displayed cycling hypoxia to a larger extent than the HT29 tumor, a feature associated with prosurvival pathways, which can confer resistance to treatment. The difference in tumor oxygenation could influence each tumor's response to irradiation. Figure 7C shows the growth curves of the nonirradiated SCCVII tumors and the fractionated 30 Gy (10×3 Gy) irradiated tumors. X-ray irradiation was started 8 days after tumor implantation. Tumor suppression was confirmed 2 days after the beginning of irradiation, and the growth was delayed for 5 days by 30 Gy of irradiation. X-ray irradiation to HT29 tumors was started 10 days after tumor implantation when the tumor size was about 700 mm³ which was comparable to that on day 8 with the SCCVII tumors. The growth kinetics of the irradiated HT29 tumors were almost same as those of the nonirradiated control
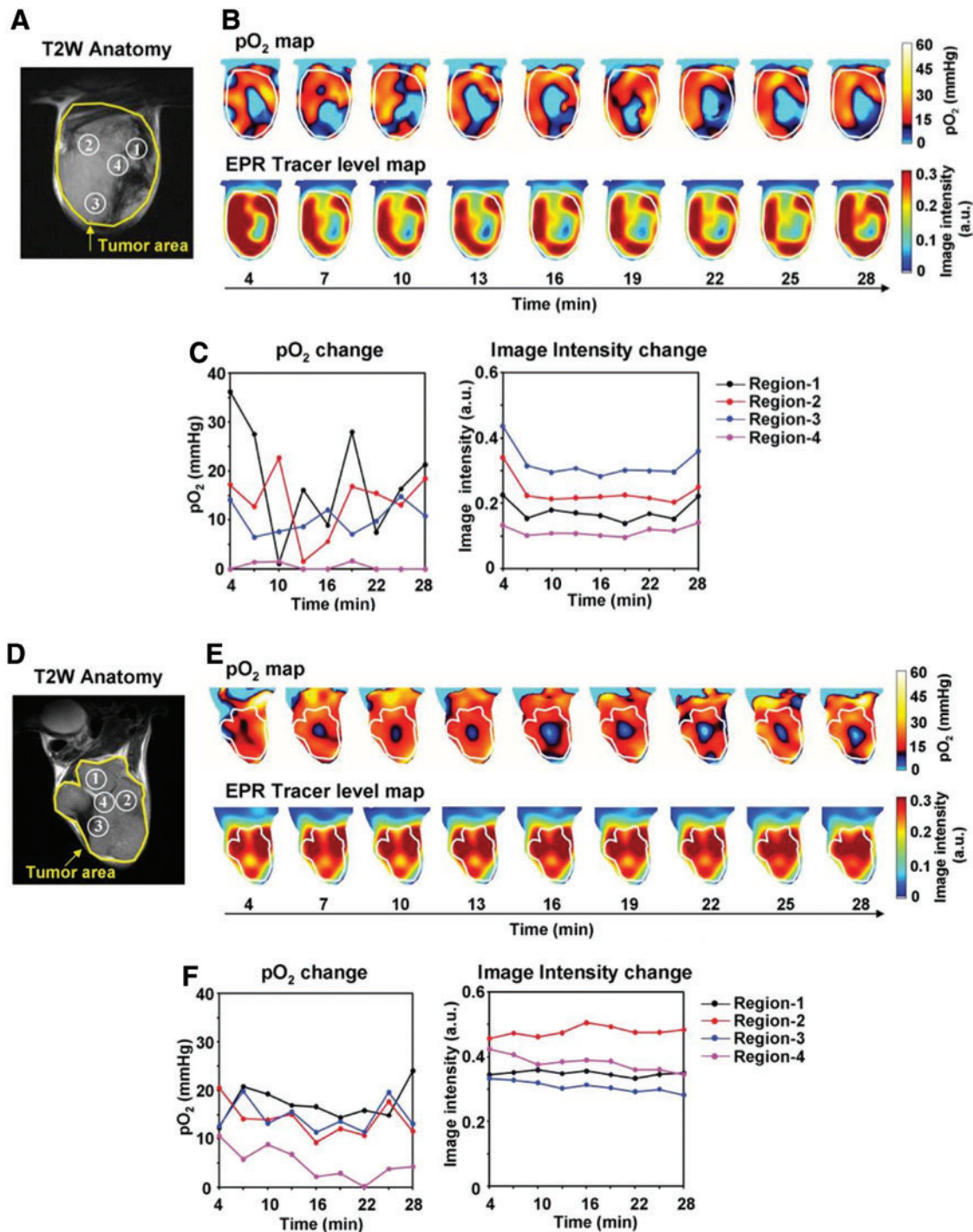
FIG. 6. Noninvasive imaging of fluctuating pO$_2$ in SCCVII (A–C) and HT29 (D–F) tumors using EPRI. (A, D) T$_2$-weighted anatomical image of a representative SCCVII tumor-bearing mouse. Large *yellow line* indicates tumor region. Four regions of interest (ROIs) indicated by small *white line* were chosen for tracing fluctuations of pO$_2$ and spin intensity with time. **(B, E)** Corresponding pO$_2$ maps (*upper panels*) and the tracer level maps (*lower panels*) were obtained from EPRI. Tumor region is shown by *white line*. Time increased from *left* to *right* from 4 to 28 min. **(C, F)** The values of pO$_2$ and the tracer level in each ROI region were quantified and plotted as a function of time. Adapted from Ref. (66) with permission. To see this illustration in color, the reader is referred to the web version of this article at www.liebertpub.com/ars

tumors until 1 day after fractionated 30 Gy irradiation, after which the tumor shrank (Fig. 7D). The difference in radiation response in these two tumors was consistent with the relatively higher median pO$_2$ of the HT29 tumors compared with the SCCVII tumors.

Hypoxia-activated prodrug. Hypoxia-activated prodrugs (HAPs) have been developed to selectively target tumor cells in hypoxic niches that are often refractory to antiproliferative agents. The most common type of HAP is based on 2-nitroimidazoles covalently linked to an alkylating nitrogen
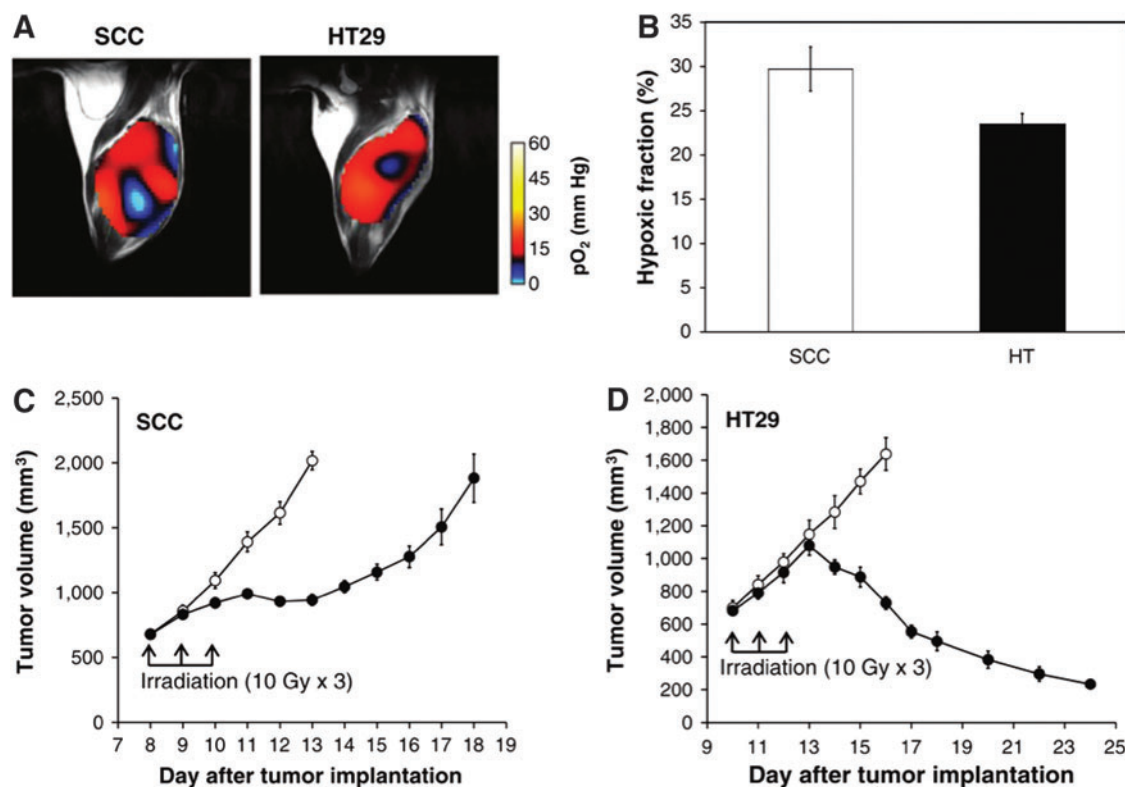
FIG. 7. Oxygen status is associated with the treatment response to radiation therapy. (A) pO_2 maps in a SCCVII tumor and a HT-29 tumor. (B) Percentage of hypoxic fraction ($pO_2 < 10$ mm Hg) in SCCVII tumors ($n=5$) and HT-29 tumors ($n=4$). (C, D) Growth curves of SCCVII ($n=7$ for each control and irradiated group) and HT-29 ($n=7$ for each control and irradiated group) with (*filled circle*) and without (*open circle*) X-irradiation. Adapted from Ref. (53) with permission. To see this illustration in color, the reader is referred to the web version of this article at www.liebertpub.com/ars

mustard, Br-isophosphoramide, as a cytotoxic effector, represented by TH-302, which is activated by cytochrome P450 reductase. Pyruvate is reported to enhance the mitochondrial oxygen consumption and create the temporary hypoxic environment in several types of tumor xenograft (61, 65). To verify that pyruvate-induced hypoxia will potentiate the antitumor effect of TH-302, a serial acquisition of intratumor oxygen mapping after pyruvate injection was performed (48, 61, 65). Figure 8A and B shows the effect of pyruvate on inducing hypoxia in three cell lines of pancreatic ductal adenocarcinoma-bearing mouse models. Pyruvate (1.15 mmol/kg) was administered i.v. and tumor pO_2 was recorded and presented as HF10 (pixels <10 mmHg) of the entire tumor region. In SU.86.86 and Hs766t tumors, the greatest decrease in pO_2 was observed 30 min after injection, followed by recovery within 60 min (Fig. 8A). In MiaPaCa-2 tumors, the pO_2 continued to decline throughout the experiments without recovery. The HF10 increased significantly in both MiaPaCa-2 (22%) and Hs766t (12%) tumors, whereas SU.86.86 showed only 7% increase 30 min after administering pyruvate (Fig. 8B). Representative histograms of tumor pO_2 demonstrate a significantly decreased pO_2 after pyruvate administration in Hs766t and MiaPaCa-2 tumors with an increased percentage of HF10. Figure 8C and D shows the enhanced therapeutic effect of TH-302 induced by pyruvate injection, causing temporary hypoxia. Mice were randomly assigned into three treatment groups: (i) saline control, (ii) TH-302 alone, and (iii) pyruvate+TH-302

(pyruvate 30 min before TH-302). Pyruvate injection did not show any benefit in survival in SU.86.86 tumors, which were resistant to TH-302 alone (Fig. 8D, E). This was probably because they were still well oxygenated even after pyruvate pretreatment. However, pyruvate injection significantly prolonged Hs766t survival time (Fig. 8D, E) with 50% of the animals surviving beyond 54 days, at which time all animals with other tumors in the study reached an endpoint. Pyruvate injection induced the greatest decrease in tumor pO_2 in MiaPaCa-2 tumors (Fig. 8A). Such tumors exhibited a significant delay in tumor growth by pyruvate injection compared with both saline control and TH-302 monotherapy groups. By injecting pyruvate before TH-302 treatment, the time to reach 2000 mm^3 was significantly prolonged compared with that of the TH-302 monotherapy group ($p < 0.05$), and overall survival also significantly increased by 9.7 days ($p < 0.005$ in the pyruvate+TH-302 treatment group compared with saline control group) (log rank $p < 0.05$) (Fig. 8C, D). In this study, EPR oximetry could successfully predict the treatment efficacy of HAP. This suggests that it can also be applied for the purposes of developing HAPs with higher efficacy or selecting the HAPs sensitive tumors based on extent of hypoxia.

Photoimmunotherapy. Photoimmunotherapy (PIT) is a modality of photodynamic therapy in which a photosensitizer–cancer-targeting monoclonal antibody conjugate is used (18, 21, 45, 46, 56). Photochemical reactions represented by Type I
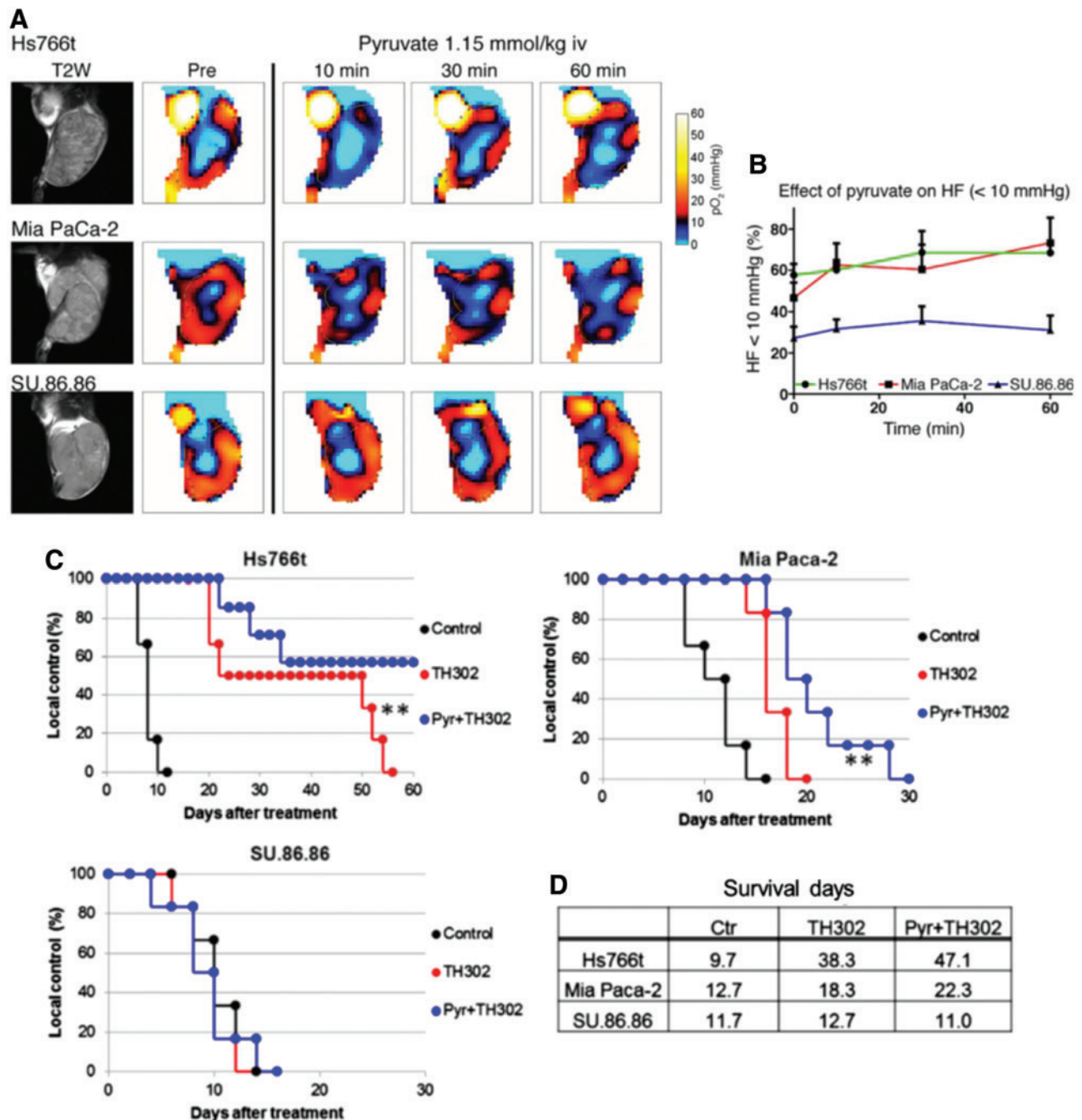
FIG. 8. EPR tumor oxygen imaging after pyruvate injection and effect of pyruvate injection on treatment outcome.
(A) EPR oxygen imaging of subcutaneous Hs766t, MiaPaCa-2, and SU.86.86 tumors pre- and post (10–60 min) i.v. pyruvate administration. Representative T_2-weighted anatomical MRI and pO_2 maps are provided in $N=4$ biological replicates per tumor type. **(B)** Temporal changes of percentage hypoxic fraction (<10 mmHg) of pyruvate-treated pancreatic ductal adenocarcinoma tumors. Data are presented as mean ± SD. Proposed histological predictive biomarkers for pyruvate sensitivity. **(C)** Local tumor control (%) of Hs766t, MiaPaCa-2, and SU.86.86 tumors treated with saline, TH-302 alone (80 mg/kg·5 days I.P.), or TH-302 following a 30 min pretreatment with exogenous pyruvate (1.15 mmol/kg pyruvate i.v. 30 min before 80 mg/kg TH-302 I.P.·5 days). Response was measured as percentage of surviving animals as mice are removed from study when tumors reach 2000 mm³. Pyruvate pretreatment significantly improved local control of Hs766t ($p < 0.00225$) and MiaPaCa-2 tumors with no measurable effect against SU.86.86. **(D)** Mean survival (days) of mice with pancreatic tumors treated with TH-302 and TH-302 in combination with pyruvate pretreatment. $N=10$ mice per treatment group. A two-tailed Student's *t*-test was used to determine significance. **$p < 0.01$. Adapted from Ref. (65) with permission. To see this illustration in color, the reader is referred to the web version of this article at www.liebertpub.com/ars
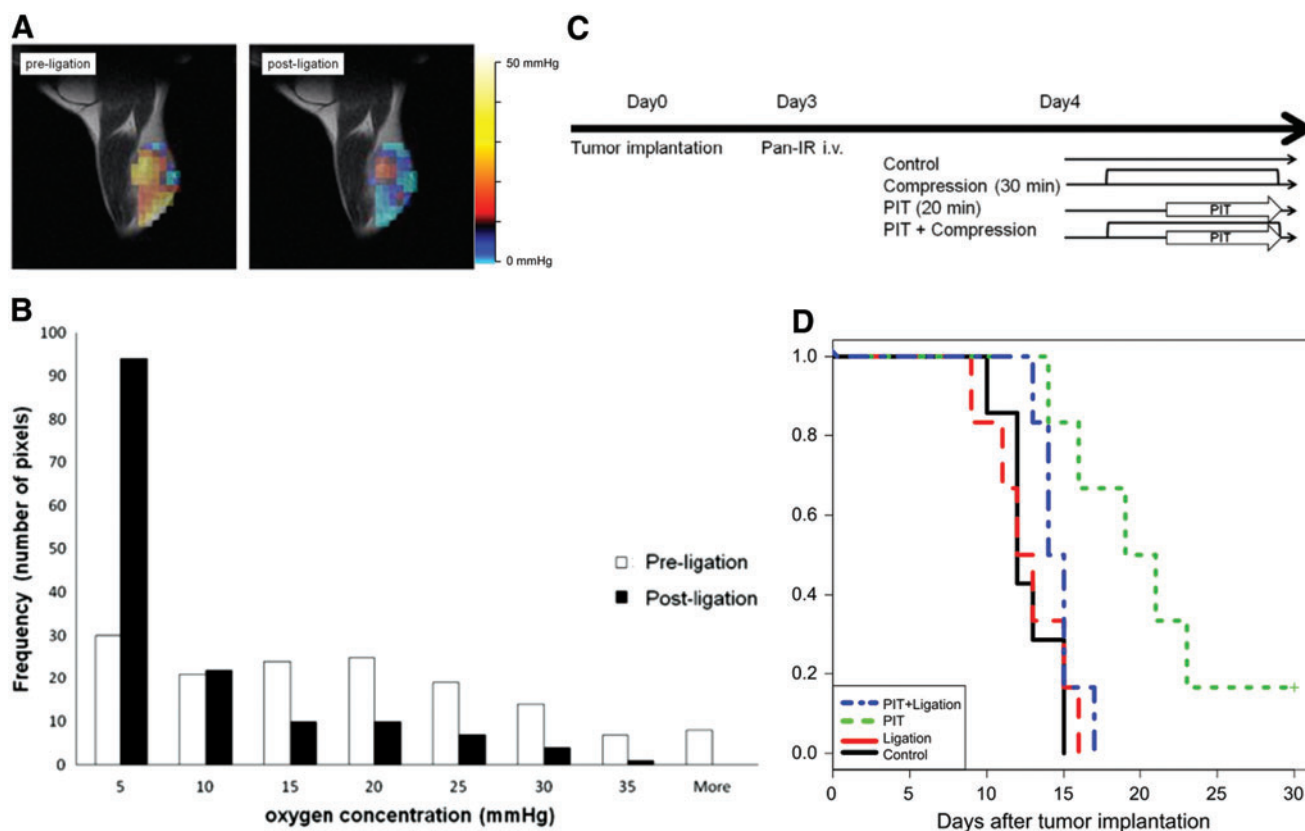
FIG. 9. Inguinal ligation with rubber band-induced focal hypoxia and effect of hypoxia induction on treatment outcome of PIT. (A) Representative EPR images of tumor pre- and postligation. **(B)** Histogram of pixel values of intratumor pO_2. Pre- (*open bar*) and postligation (*filled bar*) ($n = 3$). Results are mean ± SD. **(C)** Schematic of treatments for each group. **(D)** Kaplan–Meier plot shows inhibition of PIT effect on survival. Statistically significant difference $p < 0.05$ was observed in survival curve between PIT group and PIT+ligation group by log rank test (control group; $n = 7$, other groups; $n = 6$). PIT, photoimmunotherapy. Adapted from Ref. (29) with permission. To see this illustration in color, the reader is referred to the web version of this article at www.liebertpub.com/ars

and Type II are thought to be the main mechanisms of tumoricidal effect. To verify the oxygen-dependent antitumor effect of PIT, a validation study for hypoxic tumor model was performed (29) using A431 tumor cell line with a high expression level of epidermal growth factor receptor. IR700, a near-infrared absorbing photosensitizer, was conjugated with panitumumab and used as the photosensitizer–immunoconjugate. The A431 tumor was implanted in the right hind leg and proximal part was compressed by a rubber band to create hypoxia in the tumor. After rubber band compression was applied for 30 min to shut down the blood supply to the tumor, quantitative pO_2 changes in tumor pO_2 in response to the intervention were monitored by EPRI. Figure 9A shows pO_2 maps in the A431 tumor-implanted leg taken by EPRI after the injection of paramagnetic tracer Oxo63. The pO_2 maps before compression (left) show well-oxygenated tumor with focal hypoxic regions. When the tumor pO_2 was obtained 30 min after compression, a global pO2 reduction was monitored. The histogram of pO_2 showed significant decrease in the tumor after hypoxia induction by compression. The median drop in pO_2 postligation was >10 mmHg (Fig. 9B). Figure 9C is the scheme of PIT with the photoimmunoconjugate treatment on four groups of A431 tumor-bearing mice. Figure 9D shows the effect of hypoxia on treatment response to PIT. The Kaplan–Meier survival curve shows the diminished thera-

peutic effects of PIT by inducing hypoxia in tumor, supporting the oxygen dependency of therapeutic effect of PIT.

Coregistration with other imaging modalities

When intratumor pO_2 is decreased, there is an abnormal balance between oxygen delivery and consumption in the tumor. Thus, to understand the change in oxygenation, the assessment of closely related factors such as blood perfusion (oxygen supply) or tumor metabolic profiles (oxygen consumption) provides causative information for hypoxia. In general, tumor size/stage largely affects the tumor physiology, resulting in altered response to cancer therapy.

Blood volume imaging. Tumor blood vessels are known to have immature blood vessels with inadequate pericyte coverage (27, 43, 47), resulting in enhanced capillary leak and ineffective oxygen delivery. It has been reported that the tumor hypoxia and its poor vascularity are associated with larger tumor size (22, 55). The blood volume can be examined using the blood pool T_2^* contrast agent ultrasmall superparamagnetic iron oxide particles (USPIO). By comparing the blood volume imaging with EPRI, it is feasible to investigate the relationship between tumor size, hypoxic area, and its vascularity. Figure 10A shows the tumor pO_2 maps
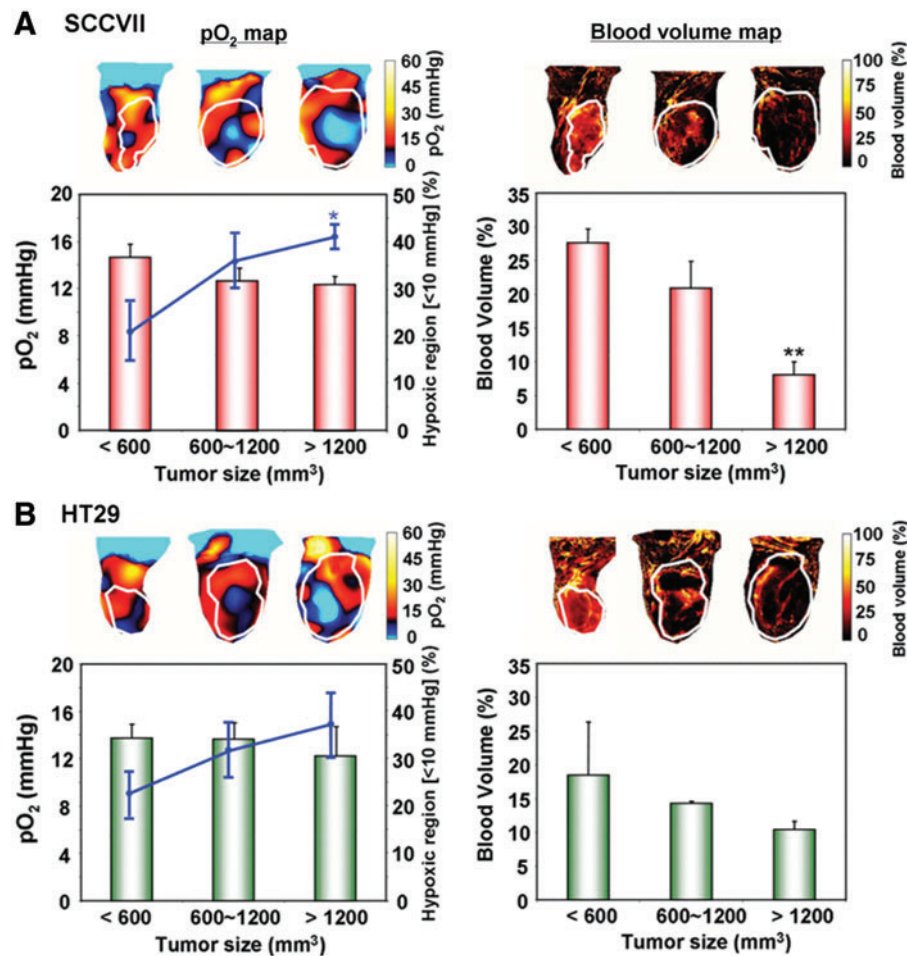
FIG. 10. The effects of tumor type and size on oxygenation and blood volume. Median tumor pO_2 and the percentage of hypoxic region were estimated from EPRI in **(A)** SCCVII and **(B)** HT29 tumors. Representative pO_2 maps at three tumor sizes are shown in the *left upper panels*. Tumor pO_2 values from at least three tumors at each size are shown in *red bar* graphs ($n = 3$–4). The hypoxic volume, the percentage of the tumor volume having pO_2 <10 mmHg, was plotted as a *line* superimposed on the bar graphs ($n = 3$–4). Blood volume images (*right panels*) were obtained from MRI studies using USPIO ($n = 3$–4). MRI, magnetic resonance imaging; USPIO, ultrasmall superparamagnetic iron oxide particles. *$p < 0.05$. **$p < 0.01$. Adapted from Ref. (66) with permission. To see this illustration in color, the reader is referred to the web version of this article at www.liebertpub.com/ars

taken by EPRI and blood volume imaging taken by MRI using USPIO in a representative SCCVII tumor (66). The EPR oxygen maps showed that the averaged tumor pO_2 was negatively correlated with the tumor size. The pO_2 levels were 14.8 ± 1.1, 12.7 ± 1.1, and 12.4 ± 0.7 mmHg for the small, medium, and large tumor, respectively. HF10 was higher in the largest tumor ($41.0\% \pm 2.6\%$) than HF10 in the

small tumor ($20.9\% \pm 6.2\%$). Small tumors were uniformly covered by blood vessels with a density of $27.7\% \pm 2.1\%$ compared with the large tumors displaying significant heterogeneity, and their density was $8.1\% \pm 2.0\%$. Similar tendency in blood vessel density and pO_2 was also observed in HT29 tumors, although not statistically significant (Fig. 10B).
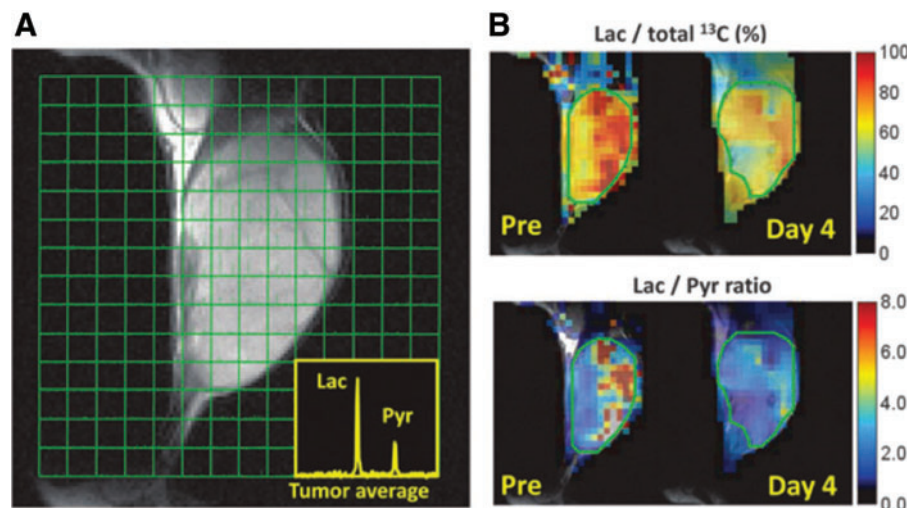

FIG. 11. pO_2 images in SCCVII tumors before and after sunitinib treatment. Longitudinal and three-dimensional EPR oxygen images (*top*). **(A)** ^{13}C spectroscopic images of exogenously injected 1-^{13}C-pyruvate metabolism in an SCCVII tumor. *Insets* are ^{13}C MR spectra averaged over tumor regions. **(B)** Artificial images of lactate-to-total ^{13}C (*top*) and lactate-to-pyruvate ratios (*bottom*) calculated from the spectroscopic images. Adapted from Ref. (41) with permission. To see this illustration in color, the reader is referred to the web version of this article at www.liebertpub.com/ars

FIG. 12. Comparison of tumor pO_2 and MCT1 expression. After EPR oxygen imaging and after anatomic MRI scans, tumor tissue slice corresponding to the particular slice of *in vivo* pO_2 map was excised, and immunostaining of HIF-1a (*blue*) and MCT1 (*red*) was conducted. Adapted from Ref. (42) with permission. To see this illustration in color, the reader is referred to the web version of this article at www.liebertpub.com/ars
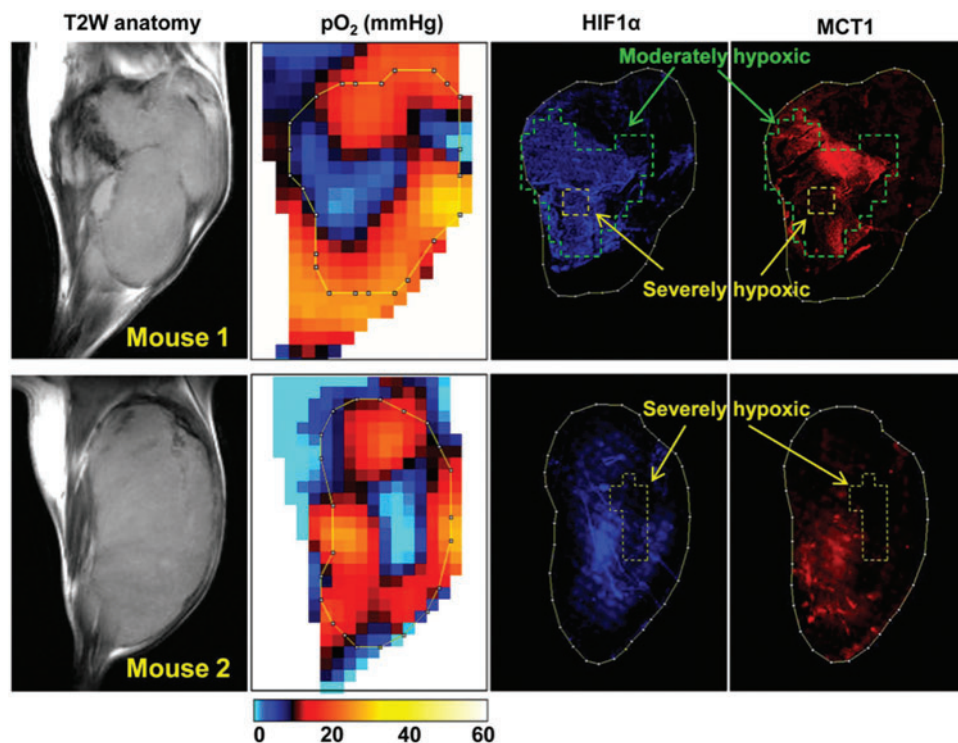
Metabolic imaging. The metabolic profile of tumor can be obtained using a relatively new technique, known as hyperpolarized ^{13}C MRI. By hyperpolarizing ^{13}C nuclei *via* dynamic nuclear polarization, it is possible to enhance the ^{13}C signal by four orders in magnitude to obtain magnetic resonance spectroscopy imaging (12, 23, 25). Pyruvate is at a critical junction of energy metabolism and can proceed to either lactate (glycolysis) or TCA cycle (oxidative phosphorylation). By using $^{13}C_1$-labeled pyruvate as a probe, metabolic profiling of tumor cell is possible after injecting $^{13}C_1$ pyruvate and monitoring its conversion to $^{13}C_1$ lactate (1). Tumor cells exhibit aerobic glycolysis also known as Warburg phenomenon for glucose metabolism and produce as much as 50% of their ATP by converting pyruvate to lactate even in the presence of oxygen (17, 64). Besides, normal tissue is known to produce most of ATP in mitochondria by an oxygen-dependent pathway wherein glucose is eventually converted to CO_2 and water. Although the shift in energy production is regulated by extremely complex pathways, the resultant upregulation of glucose uptake and aerobic glycolysis offers an opportunity for diagnoses and treatments in cancer therapy (17). Especially the cancer cells located in hypoperfused and hypoxic regions show even higher rate of aerobic glycolysis for energy production due to survival with limited amount of oxygen (66). Thus, the metabolic profile and pO_2 status may be related to each other. Figure 11 shows an example of hyperpolarized ^{13}C MRI metabolic imaging taken from SCCVII tumor (41). The ^{13}C MRI was obtained 30 s after the intravenous injection of hyperpolarized $^{13}C_1$ pyruvate into SCCVII tumor-bearing mice. The injected pyruvate is rapidly converted to lactate, and a strong lactate peak is observed in the tumor region (Fig. 11A). Parametrically generated lactate-to-pyruvate ratio maps can visually demonstrate the heterogeneous distribution of the lactate-to-pyruvate ratio (Fig. 11B). Although the image resolution of metabolic imaging is >2 mm, the extent of aerobic glycolysis in the tumor can be estimated.

Histochemical analysis. To further examine the relationship between hypoxic phenotype and gene expression in the same tumor, immunohistochemical analysis can be combined with EPR oximetry. Since EPR oximetry provides three-dimensional pO_2 maps, the excised tissue can easily be geometrically coregistered and stained with various antibodies. Figure 12 shows pO_2 image-guided histological experiments in which different types of biphasic oxygen dependency between MCT1 and HIF-1a expression were observed (42). In moderately hypoxic regions in the tumor ($pO_2 = 5–15$ mmHg, marked by green line) surrounding a severely hypoxic core (yellow line), increased expression of MCT1 as well as overexpression of HIF-1a was observed. However, the expression level of MCT1 was clearly decreased in the severely hypoxic tumor regions, especially where pO_2 was <2–3 mmHg, whereas HIF-1 expression was high even in severely hypoxic regions when the severely hypoxic area was relatively small (mouse 1). When the size of severely hypoxic regions were beyond 2–3 mm (mouse 2), the expression level of HIF-1 was decreased, consistent with the biphasic HIF-1 expression pattern near necrosis in a tumor reported in both preclinical models and human tumors in previous studies. Of note, a decrease in the MCT1 expression in the severely hypoxic regions was apparent compared with that of HIF-1a, and the MCT1 expression was almost diminished in the tumor regions with pO_2 <8–12 mmHg. The heterogeneous hypoxia-related protein expression levels inside of the tumor can be examined with actual hypoxic region evaluated by EPR oximetry.
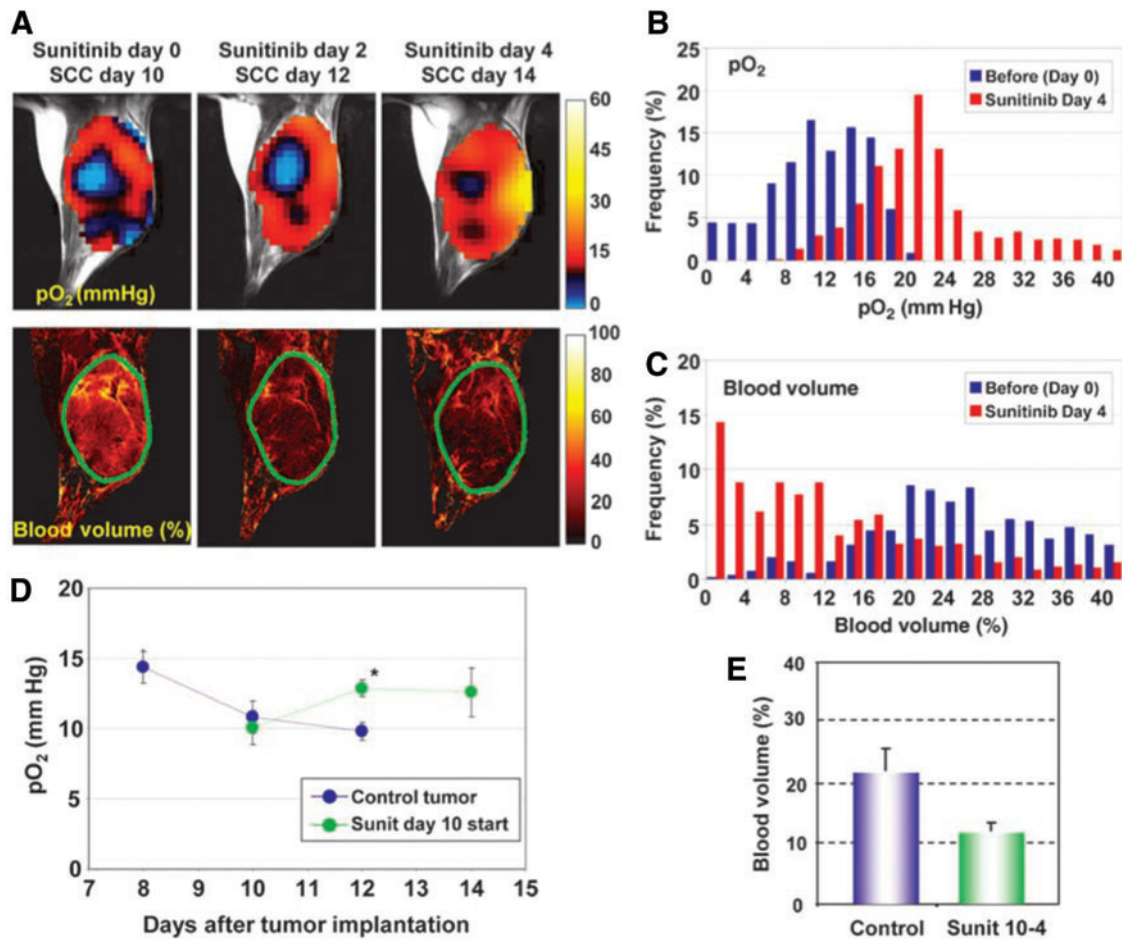
FIG. 13. **Tumor pO$_2$ and blood volume imaging before and after antiangiogenic treatment initiated at the later stage of tumor.** **(A)** Initiation of antiangiogenic treatment at the later stage of tumor improved tumor oxygenation (*top*) and reduced tumor blood volume (*bottom*) without a significant change in tumor size. The tumors were plotted by *green lines*. **(B, C)** Frequency histograms (percentage of voxels with a given pO$_2$ and blood volume) before and 4 days after antiangiogenic treatment showed a clear right shift in pO$_2$ but a shift in blood volume. **(D)** Quantitation of pO$_2$ changes in sunitinib-treated and control mice. *$p < 0.05$. **(E)** Tumor blood volume decreased ∼45% 4 days after treatment initiated at the later stage of tumor. Sunit, sunitinib. Sunit 10-4, fourth day after treatment of a tumor 10 days after implantation. Adapted from Ref. (39) with permission. To see this illustration in color, the reader is referred to the web version of this article at www.liebertpub.com/ars

Treatment response

The early detection of treatment response in cancer is useful to select and customize the therapeutic strategy to cancer. Although computed tomography or MRI can be utilized to indirectly observe the morphological changes, it usually takes time to show a detectable change and the assessment of quantitative change is difficult. Since EPR is the method for direct mapping of quantitative pO$_2$ measurement, the treatment response can be observed and tracked over time by EPR oximetry which is influenced by the metabolic or perfusion change. Figure 13 shows the treatment response in oxygen maps to vascular endothelial growth factor (VEGF) inhibitor sunitinib (39). Figure 13A shows the change in intratumor oximetry after sunitinib treatment using SCCVII murine carcinoma model. Mice were treated daily with oral administration of 50 mg/kg sunitinib. Interestingly, in the study, the improved intratumor oxygenation was observed at days 4 and 6 after sunitinib treatment (Fig. 13B, D), although the blood volume decreased (Fig. 13C, E). This explains the

paradox that many previous studies indicated a significant survival benefit in patients when VEGF inhibitors are combined with other chemotherapies or radiotherapy, although these drugs are likely to decrease blood delivery and other chemotherapies resulting in decreased efficacy of the treatment. This transient oxygenation after antiangiogenic therapy is known as ''vascular normalization'' process where the immature vessels are pruned while the rest mature into structurally competent vessels with improved function. Mammalian target of rapamycin (mTOR) inhibitor, rapamycin, was also examined by a similar technique and was found to have a vascular normalization process (54), which is consistent with the previous report of the antiangiogenic effects of rapamycin observed in a tumor-bearing mouse model, showing decreased VEGF production and resistance of endothelial cells to VEGF stimulation (32). By clarifying the kinetics of oxygenation in such a manner, EPR can lead to effective combination therapies with oxygen-dependent therapy such as radiotherapy with hypoxia-activated prodrugs such as TH-302.

Conclusions

The development of EPR oximetry allowed studying the intratumor pO_2 kinetics quantitatively. Since the hypoxia in tumors is associated with malignancy, therapy resistance, and metastasis, it is of great importance to monitor pO_2 in the tumors. Combining EPR oximetry with various other imaging techniques or histological analyses is also useful to elucidate the heterogeneous intratumor metabolism. It will further help developing and optimizing the therapies whose effect is dependent on pO_2 in the tumor.

Acknowledgment

References

1. Albers MJ, Bok R, Chen AP, Cunningham CH, Zierhut ML, Zhang VY, Kohler SJ, Tropp J, Hurd RE, Yen Y-F, Nelson SJ, Vigneron DB, and Kurhanewicz J. Hyperpolarized 13C lactate, pyruvate, and alanine: noninvasive biomarkers for prostate cancer detection and grading. *Cancer Res* 68: 8607–8615, 2008.

2. Alecci M, Della Penna S, Sotgiu A, Testa L, and Vannucci I. Electron paramagnetic resonance spectrometer for three-dimensional in vivo imaging at very low frequency. *Rev Sci Instrum* 63: 4263–4270, 1992.

3. Ardenkjær-Larsen JH, Laursen I, Leunbach I, Ehnholm G, Wistrand L-G, Petersson JS, and Golman K. EPR and DNP properties of certain novel single electron contrast agents intended for oximetric imaging. *J Magn Reson* 133: 1–12, 1998.

4. Bentzen L, Keiding S, Horsman MR, Grönroos T, Hansen SB, and Overgaard J. Assessment of hypoxia in experimental mice tumours by [18 F] fluoromisonidazole PET and pO2 electrode measurements. *Acta Oncol* 41: 304–312, 2002.

5. Brown JM. Evidence for acutely hypoxic cells in mouse tumours, and a possible mechanism of reoxygenation. *Br J Radiol* 52: 650–656, 1979.

6. Buxton RB. The physics of functional magnetic resonance imaging (fMRI). *Rep Prog Phys* 76: 96601, 2013.

7. Crawford JH. Hypoxia, red blood cells, and nitrite regulate NO-dependent hypoxic vasodilation. *Blood* 107: 566–574, 2006.

8. Dewhirst MW. Intermittent hypoxia furthers the rationale for hypoxia-inducible factor-1 targeting. *Cancer Res* 67: 854–855, 2007.

9. Dewhirst MW. Relationships between cycling hypoxia, HIF-1, angiogenesis and oxidative stress. *Radiat Res* 172: 653–665, 2009.

10. Dewhirst MW, Cao Y, and Moeller B. Cycling hypoxia and free radicals regulate angiogenesis and radiotherapy response. *Nat Rev Cancer* 8: 425–437, 2008.

11. Dewhirst MW, Ong ET, Braun RD, Smith B, Klitzman B, Evans SM, and Wilson D. Quantification of longitudinal tissue pO_2 gradients in window chamber tumours: impact on tumour hypoxia. *Br J Cancer* 79: 1717–1722, 1999.

12. Durand RE and Aquino-Parsons C. Clinical relevance of intermittent tumour blood flow. *Acta Oncol* 40: 929–936, 2001.

13. Epstein FH and Hsia CCW. Respiratory function of hemoglobin. *N Engl J Med* 338: 239–248, 1998.

14. This reference has been deleted.

15. Gallez B, Baudelet C, and Jordan BF. Assessment of tumor oxygenation by electron paramagnetic resonance: principles and applications. *NMR Biomed* 17: 240–262, 2004.

16. Gallez B and Mäder K. Accurate and sensitive measurements of pO_2 in vivo using low frequency EPR spectroscopy: how to confer biocompatibility to the oxygen sensors. *Free Radic Biol Med* 29: 1078–1084, 2000.

17. Gatenby RA and Gillies RJ. Why do cancers have high aerobic glycolysis? *Nat Rev Cancer* 4: 891–899, 2004.

18. Goff BA, Bamberg M, and Hasan T. Photoimmunotherapy of human ovarian carcinoma cells ex vivo. *Cancer Res* 51: 4762–4767, 1991.

19. Halpern HJ, Spencer DP, van Polen J, Bowman MK, Nelson AC, Dowey EM, and Teicher BA. Imaging radio frequency electron-spin-resonance spectrometer with high resolution and sensitivity for in vivo measurements. *Rev Sci Instrum* 60: 1040–1050, 1989.

20. Halpern HJ, Yu C, Peric M, Barth E, Grdina DJ, and Teicher BA. Oxymetry deep in tissues with low-frequency electron paramagnetic resonance. *Proc Natl Acad Sci U S A* 91: 13047–13051, 1994.

21. Hamblin MR, Miller JL, and Hasan T. Effect of charge on the interaction of site-specific photoimmunoconjugates with human ovarian cancer cells. *Cancer Res* 56: 5205–5210, 1996.

22. Hendriksen E, Span P, Schuuring J, Peters JPW, Sweep FCGJ, van der Kogel AJ, and Bussink J. Angiogenesis, hypoxia and VEGF expression during tumour growth in a human xenograft tumour model. *Microvasc Res* 77: 96–103, 2009.

23. Hockel M, Schlenger K, Aral B, Mitze M, Schaffer U, and Vaupel P. Association between tumor hypoxia and malignant progression in advanced cancer of the uterine cervix. *Cancer Res* 56: 4509–4515, 1996.

24. Hockel M and Vaupel P. Tumor hypoxia: definitions and current clinical, biologic, and molecular aspects. *J Natl Cancer Inst* 93: 266–276, 2001.

25. Horsman MR, Nordsmark M, and Overgaard J. Techniques to assess the oxygenation of human tumors. State of the art. *Strahlenther Onkol* 174(Suppl 4): 2–5, 1998.

26. This reference has been deleted.

27. Jain RK. A new target for tumor therapy. *N Engl J Med* 360: 2669–2671, 2009.

28. This reference has been deleted.

29. Kishimoto S, Bernardo M, Saito K, Koyasu S, Mitchell JB, Choyke PL, and Krishna MC. Evaluation of oxygen dependence on in vitro and in vivo cytotoxicity of photoimmunotherapy using IR-700–antibody conjugates. *Free Radic Biol Med* 85: 24–32, 2015.

30. Krishna MC, English S, Yamada K, Yoo J, Murugesan R, Devasahayam N, Cook JA, Golman K, Ardenkjaer-Larsen JH, Subramanian S, and Mitchell JB. Overhauser enhanced magnetic resonance imaging for tumor oximetry: coregistration of tumor anatomy and tissue oxygen concentration. *Proc Natl Acad Sci U S A* 99: 2216–2221, 2002.

31. Kuppusamy P, Chzhan M, Vij K, Shteynbuk M, Lefer DJ, Giannella E, and Zweier JL. Three-dimensional spectral-spatial EPR imaging of free radicals in the heart: a technique for imaging tissue metabolism and oxygenation. *Proc Natl Acad Sci U S A* 91: 3388–3392, 1994.

32. Lane HA, Wood JM, McSheehy PMJ, Allegrini PR, Boulay A, Brueggen J, Littlewood-Evans A, Maira S-M, Martiny-Baron G, Schnell CR, Sini P, and O'Reilly T. mTOR in-

hibitor RAD001 (everolimus) has antiangiogenic/vascular properties distinct from a VEGFR tyrosine kinase inhibitor. *Clin Cancer Res* 15: 1612–1622, 2009.

33. Liu KJ, Gast P, Moussavi M, Norby SW, Vahidi N, Walczak T, Wu M, and Swartz HM. Lithium phthalocyanine: a probe for electron paramagnetic resonance oximetry in viable biological systems. *Proc Natl Acad Sci U S A* 90: 5438–5442, 1993.

34. Maltempo MM. Differentiation of spectral and spatial components in EPR imaging using 2-D image reconstruction algorithms. *J Magn Reson* 69: 156–161, 1986.

35. Maltempo MM, Eaton SS, and Eaton GR. Reconstruction of spectral-spatial two-dimensional EPR images from incomplete sets of projections without prior knowledge of the component spectra. *J Magn Reson* 77: 75–83, 1988.

36. Matsumoto A, Matsumoto K, Matsumoto S, Hyodo F, Sowers AL, Koscielniak JW, Devasahayam N, Subramanian S, Mitchell JB, and Krishna MC. Intracellular hypoxia of tumor tissue estimated by noninvasive electron paramagnetic resonance oximetry technique using paramagnetic probes. *Biol Pharm Bull* 34: 142–145, 2011.

37. Matsumoto K, Bernardo M, Subramanian S, Choyke P, Mitchell JB, Krishna MC, and Lizak MJ. MR assessment of changes of tumor in response to hyperbaric oxygen treatment. *Magn Reson Med* 56: 240–246, 2006.

38. Matsumoto K, Subramanian S, Devasahayam N, Aravalluvan T, Murugesan R, Cook JA, Mitchell JB, and Krishna MC. Electron paramagnetic resonance imaging of tumor hypoxia: enhanced spatial and temporal resolution for in vivo pO2 determination. *Magn Reson Med* 55: 1157–1163, 2006.

39. Matsumoto S, Batra S, Saito K, Yasui H, Choudhuri R, Gadisetti C, Subramanian S, Devasahayam N, Munasinghe JP, Mitchell JB, and Krishna MC. Antiangiogenic agent sunitinib transiently increases tumor oxygenation and suppresses cycling hypoxia. *Cancer Res* 71: 6350–6359, 2011.

40. Matsumoto S, Hyodo F, Subramanian S, Devasahayam N, Munasinghe J, Hyodo E, Gadisetti C, Cook JA, Mitchell JB, and Krishna MC. Low-field paramagnetic resonance imaging of tumor oxygenation and glycolytic activity in mice. *J Clin Invest* 118: 1965–1973, 2008.

41. Matsumoto S, Saito K, Takakusagi Y, Matsuo M, Munasinghe JP, Morris HD, Lizak MJ, Merkle H, Yasukawa K, Devasahayam N, Suburamanian S, Mitchell JB, and Krishna MC. In vivo imaging of tumor physiological, metabolic, and redox changes in response to the antiangiogenic agent sunitinib: longitudinal assessment to identify transient vascular renormalization. *Antioxid Redox Signal* 21: 1145–1155, 2014.

42. Matsumoto S, Saito K, Yasui H, Morris HD, Munasinghe JP, Lizak M, Merkle H, Ardenkjaer-Larsen JH, Choudhuri R, Devasahayam N, Subramanian S, Koretsky AP, Mitchell JB, and Krishna MC. EPR oxygen imaging and hyperpolarized ^{13}C MRI of pyruvate metabolism as noninvasive biomarkers of tumor treatment response to a glycolysis inhibitor 3-bromopyruvate. *Magn Reson Med* 69: 1443–1450, 2013.

43. Matsumoto S, Yasui H, Batra S, Kinoshita Y, Bernardo M, Munasinghe JP, Utsumi H, Choudhuri R, Devasahayam N, Subramanian S, Mitchell JB, and Krishna MC. Simultaneous imaging of tumor oxygenation and microvascular permeability using Overhauser enhanced MRI. *Proc Natl Acad Sci U S A* 106: 17898–17903, 2009.

44. Matsumoto S, Yasui H, Mitchell JB, and Krishna MC. Imaging cycling tumor hypoxia. *Cancer Res* 70: 10019–10023, 2010.

45. Mew D, Wat CK, Towers GH, and Levy JG. Photoimmunotherapy: treatment of animal tumors with tumorspecific monoclonal antibody-hematoporphyrin conjugates. *J Immunol* 130: 1473–1477, 1983.

46. Mitsunaga M, Ogawa M, Kosaka N, Rosenblum LT, Choyke PL, and Kobayashi H. Cancer cell–selective in vivo near infrared photoimmunotherapy targeting specific membrane molecules. *Nat Med* 17: 1685–1691, 2011.

47. Naumov GN, Akslen LA, and Folkman J. Role of angiogenesis in human tumor dormancy: animal models of the angiogenic switch. *Cell Cycle* 5: 1779–1787, 2006.

48. Naz S, Krishna MC, and Mitchell JB. Application of functional molecular imaging in radiation oncology. In: *Increasing the Therapeutic Ratio of Radiotherapy*, edited by Tofilon B, Camphausen K. Cancer Drug Discovery and Development. Humana Press, Cham: Humana Press, pp. 103–134.

49. Ndubuizu O and LaManna JC. Brain tissue oxygen concentration measurements. *Antioxid Redox Signal* 9: 1207–1220, 2007.

50. Noseworthy MD, Bulte DP, and Alfonsi J. BOLD magnetic resonance imaging of skeletal muscle. *Semin Musculoskelet Radiol* 7: 307–316, 2003.

51. Ogawa S, Lee TM, Kay AR, and Tank DW. Brain magnetic resonance imaging with contrast dependent on blood oxygenation. *Proc Natl Acad Sci U S A* 87: 9868–9872, 1990.

52. Rasey JS, Koh WJ, Evans ML, Peterson LM, Lewellen TK, Graham MM, and Krohn KA. Quantifying regional hypoxia in human tumors with positron emission tomography of [^{18}F]fluoromisonidazole: a pretherapy study of 37 patients. *Int J Radiat Oncol Biol Phys* 36: 417–428, 1996.

53. Saito K, Matsumoto S, Takakusagi Y, Matsuo M, Morris HD, Lizak MJ, Munasinghe JP, Devasahayam N, Subramanian S, Mitchell JB, and Krishna MC. ^{13}C-MR spectroscopic imaging with hyperpolarized [1-13C]pyruvate detects early response to radiotherapy in SCC tumors and HT-29 tumors. *Clin Cancer Res* 21: 5073–5081, 2015.

54. Saito K, Matsumoto S, Yasui H, Devasahayam N, Subramanian S, Munasinghe JP, Patel V, Gutkind JS, Mitchell JB, and Krishna MC. Longitudinal imaging studies of tumor microenvironment in mice treated with the mTOR inhibitor rapamycin. *PLoS One* 7: e49456, 2012.

55. Sorg BS, Moeller BJ, Donovan O, Cao Y, and Dewhirst MW. Hyperspectral imaging of hemoglobin saturation in tumor microvasculature and tumor hypoxia development. *J Biomed Opt* 10: 44004, 2005.

56. Soukos NS, Hamblin MR, Keel S, Fabian RL, Deutsch TF, and Hasan T. Epidermal growth factor receptor-targeted immunophotodiagnosis and photoimmunotherapy of oral precancer in vivo. *Cancer Res* 61: 4490–4496, 2001.

57. Stratford IJ, Adams GE, Bremner JC, Cole S, Edwards HS, Robertson N, and Wood PJ. Manipulation and exploitation of the tumour environment for therapeutic benefit. *Int J Radiat Biol* 65: 85–94, 1994.

58. Subramanian S, Devasahayam N, Murugesan R, Yamada K, Cook J, Taube A, Mitchell JB, Lohman JAB, and Krishna MC. Single-point (constant-time) imaging in radiofrequency Fourier transform electron paramagnetic resonance. *Magn Reson Med* 48: 370–379, 2002.

59. Subramanian S, Yamada K-I, Irie A, Murugesan R, Cook JA, Devasahayam N, Van Dam GM, Mitchell JB, and Krishna

MC. Noninvasive in vivo oximetric imaging by radio-frequency FT EPR. *Magn Reson Med* 47: 1001–1008, 2002.

60. Swartz HM and Clarkson RB. The measurement of oxygen in vivo using EPR techniques. *Phys Med Biol* 43: 1957–1975, 1998.

61. Takakusagi Y, Matsumoto S, Saito K, Matsuo M, Kishimoto S, Wojtkowiak JW, DeGraff W, Kesarwala AH, Choudhuri R, Devasahayam N, Subramanian S, Munasinghe JP, Gillies RJ, Mitchell JB, Hart CP, and Krishna MC. Pyruvate induces transient tumor hypoxia by enhancing mitochondrial oxygen consumption and potentiates the anti-tumor effect of a hypoxia-activated prodrug TH-302. *PLoS One* 9: e107995, 2014.

62. Utsumi H, Takeshita K, Miura Y, Masuda S, and Hamada A. In vivo EPR measurement of radical reaction in whole mice—influence of inspired oxygen and ischemia-reperfusion injury on nitroxide reduction. *Free Radic Res Commun* 19(Suppl 1): S219–S225, 1993.

63. Vaupel P. Oxygenation status of malignant tumors: pathogenesis of hypoxia and significance for tumor therapy. *Semin Oncol* 28: 29–35, 2001.

64. Warburg O. On the origin of cancer cells. *Science* 123: 309–314, 1956.

65. Wojtkowiak JW, Cornnell HC, Matsumoto S, Saito K, Takakusagi Y, Dutta P, Kim M, Zhang X, Leos R, Bailey KM, Martinez G, Lloyd MC, Weber C, Mitchell JB, Lynch RM, Baker AF, Gatenby RA, Rejniak KA, Hart C, Krishna MC, and Gillies RJ. Pyruvate sensitizes pancreatic tumors to hypoxia-activated prodrug TH-302. *Cancer Metab* 3: 2, 2015.

66. Yasui H, Matsumoto S, Devasahayam N, Munasinghe JP, Choudhuri R, Saito K, Subramanian S, Mitchell JB, and Krishna MC. Low-field magnetic resonance imaging to visualize chronic and cycling hypoxia in tumor-bearing mice. *Cancer Res* 70: 6427–6436, 2010.

67. Zweier JL, Thompson-Gorman S, and Kuppusamy P. Measurement of oxygen concentrations in the intact beating heart using electron paramagnetic resonance spectroscopy: a technique for measuring oxygen concentrations in situ. *J Bioenerg Biomembr* 23: 855–871, 1991.

Address correspondence to:
Prof. Murali C. Krishna
Radiation Biology Branch
Center for Cancer Research
National Cancer Institute
National Institutes of Health
Building 10, Room B3 B35
Bethesda, MD 20892-1002

E-mail: murali@helix.nih.gov

Abbreviations Used

ADC = analog–digital converter
BOLD = blood oxygen level dependent
CW = continuous wave
EPR = electron paramagnetic resonance
EPRI = electron paramagnetic resonance imaging
FID = free induction decay
FT = Fourier transform
HAPs = hypoxia-activated prodrugs
HF10 = fractional tumor volume with $pO_2 < 10$ mmHg
LW = line width
MRI = magnetic resonance imaging
PET = positron emission tomography
PIT = photoimmunotherapy
pO_2 = partial pressure of oxygen
RF = radiofrequency
SPI = single point imaging
TD = time domain
TOLD = tissue oxygen level dependent
USPIO = ultrasmall superparamagnetic iron oxide particles
VEGF = vascular endothelial growth factor